

# Measurement and Prediction of the Journal Circumferential Temperature Distribution for the Rotordynamic Morton Effect

**Xiaomeng Tong**

Mem. ASME  
Department of Mechanical Engineering,  
Texas A&M University,  
College Station, TX 77840  
e-mail: tongxiaomeng1989@tamu.edu

**Alan Palazzolo**

James J. Cain Professor  
Fellow ASME  
Department of Mechanical Engineering,  
Texas A&M University,  
College Station, TX 77840  
e-mail: a-palazzolo@tamu.edu

*The journal is the part of a shaft that is inside a fluid film bearing and is usually assumed to be circumferentially isothermal. Recent work has shown that under certain vibration conditions, a significant temperature difference ( $\Delta T$ ) can develop around the journal circumference. The  $\Delta T$  may cause the shaft to bend leading to a synchronous vibration instability problem, termed the “Morton effect” (ME). A test rig was developed to verify the asymmetric journal temperature of the ME and its prediction using a five-pad tilting pad journal bearing (TPJB) operating with an eccentric shaft to replicate a circular vibration orbit. The bearing is tested at various conditions including: supply oil temperature at 28 °C and 41 °C, bearing operating eccentricities of zero and 32% $C_b$ , and rotor speed up to 5500 rpm. The journal temperature distribution is recorded with 20 sensors located around the journal circumference, and the measurements provide a benchmark for predictions from a time transient model with the three-dimensional (3D) fluid and solid finite element method (FEM), and with a simplified ME prediction approach using only steady-state results. The test results follow the predictions exhibiting a sinusoidal-like temperature profile around the circumference with an angular lag of the hot spot location behind the high spot location (angular position on the rotor that arrives at the minimum film thickness condition each rotation) by a speed-dependent angle. Increasing the supply oil temperature reduced the journal  $\Delta T$ , while increasing the bearing operating eccentricity increased the journal  $\Delta T$ . The agreement between the test and predicted results is significantly better for the 3D FEM transient model than for the steady-state-based model in terms of journal  $\Delta T$  and hot spot position. An improved version of the latter approach is proposed and yields significantly better correlation with the test measurements. [DOI: 10.1115/1.4038104]*

## 1 Introduction

Hydrodynamic bearings are widely used in modern turbomachinery to support rotors of turbines, compressors, etc., and the thin wedge-shaped film between the rotor and bearing can develop sufficient pressure to support large external loads with relatively low friction. The viscous shearing due to the velocity gradients within the film heats both the bearing and the journal. Thermal expansion of the journal reduces the bearing clearance, especially at high-speed, and may significantly affect the bearing performance including dynamic coefficients, power loss, and stability of the system. Thermo-elasto hydrodynamic analysis takes into account both the bearing and rotor elastic deformation and improves the prediction accuracy of bearing behavior compared with the thermo-hydrodynamic analysis. Bearing temperature was found to be quite nonuniform with the loaded pad usually hotter than the unloaded ones [1,2]. The temperature variation of the shaft, nevertheless, was found to be much smaller [2] and thus was assumed to be isothermal [3], and could be predicted by either averaging the oil temperature [4] or imposing the no net-heat-flow boundary conditions on the journal–oil interface [5].

The influence of rotor circumferential temperature difference ( $\Delta T$ ) on rotordynamics was ignored until the advent of modern turbomachinery designed to operate at much higher-speed. Now the effect is often observed especially in overhung rotors supported on fluid film bearings. The asymmetric thermal expansion will bend the shaft slightly, possibly resulting in increased

vibration, which may further increase the journal  $\Delta T$ . The growing vibration may trip the machine and prohibit it from normal operation if this “positive feedback” continues. This thermally induced instability problem is called Morton effect (ME) and first appears in the pioneering works of Morton [6] and Hesseborn [7]. The ME has been frequently investigated [8–15] since Morton’s original work.

Accurate prediction of the journal temperature distribution, especially the  $\Delta T$  and the hot spot location (the hot spot is the journal circumferential position with the highest temperature), is critical in determining the potential for ME-induced instability, and for its mitigation in existing machines. The journal  $\Delta T$  helps to evaluate the magnitude of the rotor thermal bow, while the phase lag between the hot spot and high spot determines the thermal bow direction (high spot is the rotor angular position, which experiences the minimum time-averaged film thickness). Morton effect predictions generally fall into two categories: (1) the high-fidelity approach [13–16], which numerically integrates the multi-physics problem of rotordynamics, thermodynamics, fluid mechanics, and deformation in the time domain to predict the transient rotor vibration and temperature and (2) the simplified approach [12,17], which adopts an iterative linearized “influence coefficient” assumption between vibration, journal  $\Delta T$ , and thermal imbalance. The latter approach ignores the actual continuous transient behavior and instead idealizes the ME as being either synchronous stable or unstable, judged by eigenvalues of a sequential steady-state model. This approach approximates the ME as a finite sequence of steady-state problems instead of a transient phenomenon. Temperature distributions obtained in this approach are evaluated at a sequence of fixed journal positions and thus ignore the effects of journal velocity on temperature. The

Contributed by the Tribology Division of ASME for publication in the JOURNAL OF TRIBOLOGY. Manuscript received May 6, 2017; final manuscript received September 27, 2017; published online October 23, 2017. Assoc. Editor: Mihai Arghir.

simplified approach also neglects transient film temperature effects by only solving the steady-state form of the energy equation. This assumes that temperatures in the lubricant follow their sources (heat generated from viscous shear) instantaneously, neglecting the time required for heating the lubricant after, for example a maximum shear (minimum film thickness) event. Thus, the hot spot and high spot are always coincident in the steady-state energy equation solution approach. The high-fidelity approach seeks to improve the prediction accuracy and treats the actual (continuous) transient response during the ME. The influence of thermal boundary conditions, bearing clearance, bearing pad and pivot flexibility, etc., is also considered due to the ME's sensitivity to these factors. As expected, the execution time of the simplified approach is much faster than the high-fidelity approach. A comparison of both methods is provided in Sec. 5.

The difficulty of measuring temperatures in a high-speed journal has limited the number of experimental ME papers appearing in the literature. Telemetry and slip ring-based approaches are required along with a shaft motion measurement and data acquisition system. Dowson [2] used 12 thermocouples, which were located in four axial journal planes, to measure the temperature variation in both circumferential and axial direction in 1966. The maximum speed was 2000 rpm and the maximum load was 3500 lb in these measurements. The steady journal temperature variation in both directions was quite small and thus the shaft was treated as an isothermal component. The journal was in equilibrium when the measurement was performed, and thus the journal surface experienced similar heat flux and negligible  $\Delta T$  in the absence of journal whirling motion.

In 1994, de Jongh [9] tested an overhung rotor supported by tilting pad bearings to replicate the thermal instability problem observed in a compressor close to 11,500 rpm. Four resistance temperature detectors (RTDs) were equally spaced around the journal circumference. The peak–peak journal  $\Delta T$  was found to be 2 °C at 10,500 rpm and the hot spot lagged the high spot by an estimated 20 deg. The system became synchronous-unstable when the rotor was accelerated up to 11,500 rpm, with vibration continuously increasing and  $\Delta T$  growing to as high as 10 °C. In 2015, Panara et al. [18] installed eight thermocouples equally spaced around the journal circumference and a few millimeters below the journal surface. The peak–peak journal  $\Delta T$  and phase lag between the high and hot spot locations were correlated to the vibration data to extract function parameters for linking vibration and temperature. Both the temperature and phase lag were found to vary with rotor speed, viscosity, heat capacity of the lubricant, etc. They compared predictions to theory and found that accurate prediction of phase lag between the hot spot and high spot was much more difficult than journal  $\Delta T$ .

Incorrect prediction of the hot spot position and/or the journal  $\Delta T$  can deteriorate the prediction accuracy of the ME instability onset speed, considering that both parameters directly determine the shaft thermal bow magnitude and direction [19]. It was believed that a finer grid of measured temperatures was needed to more accurately benchmark journal temperature prediction tools. Thus, to improve the spatial resolution of the measured journal temperature distribution, the work in this paper utilized 20 RTDs installed around the journal circumference to give the most detailed measurement of the journal  $\Delta T$  and phase lag between the high and hot spot locations, to date. The objective of the experiment was solely to measure temperature distribution of a journal in a spinning and synchronous whirling condition, as opposed to observing an actual ME instability. The test schedule varied operating conditions including rotor speed, supply oil temperature, and bearing static eccentricity. A simulation model was developed to compare predictions with measurements and utilized a three-dimensional (3D) finite element method (FEM)-based approach with both bearing and shaft asymmetric temperature variation and thermal expansion. An outline of the paper consists of the following: Section 2 details the test rig hardware and experimental results, Sec. 3 explains the high-fidelity

prediction methodology, Sec. 4 compares the experiment and prediction, Sec. 5 discusses the simplified ME prediction approach and compares it with the high-fidelity transient method, and finally, conclusions are provided in Sec. 6.

## 2 Discussion of Experiment

**2.1 Test Rig Description.** The primary objective of the test rig is to perform a comprehensive measurement of the journal circumferential temperature distribution inside a tilting pad journal bearing (TPJB) at various operating conditions including: speed up to 5500 rpm, supply oil temperature at 28 °C and 41 °C, and bearing static eccentricity at 0 and 32%  $C_b$ . A photo and a drawing of the test rig are shown in Fig. 1, and the instrumented test shaft and tilt pad journal bearing TPJB are shown in Fig. 2. The five-pad TPJB with  $L/D=1$  and  $C_b=0.0055$  in (0.14 mm) is installed between two ball bearings. The single shaft has multiple steps and a journal instrumented with 20 RTDs equally spaced around its circumference and attached 1 mm beneath the surface. The RTD leads are routed along the hollow shaft and nearly fill the cylindrical space. The journal is intentionally machined to be eccentric with a radial offset of  $r=0.0027$  in (0.0686 mm) with respect to the global centerline of the shaft determined by the ball bearings and shown in the axial cross section view in Fig. 1.

The high radial stiffness (1.6E8 N/m per bearing) of the support ball bearings nearly produces a “pinned” condition causing the

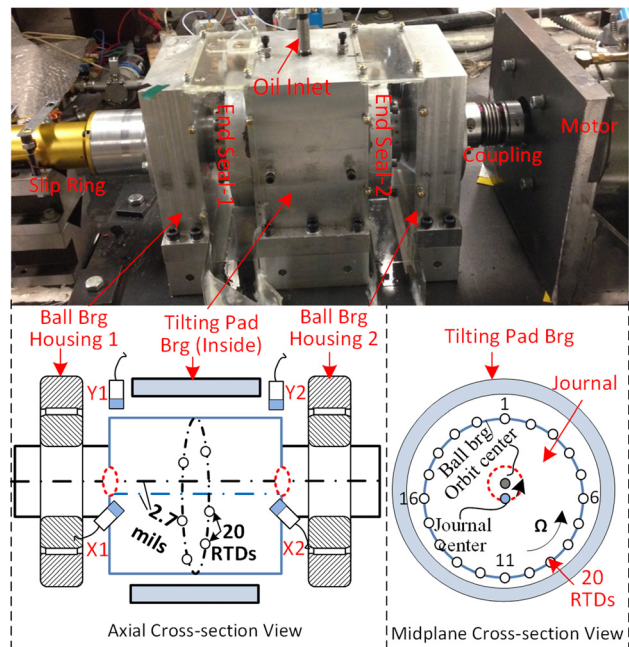


Fig. 1 Photo and diagram showing the key components of the TPJB-ME test rig

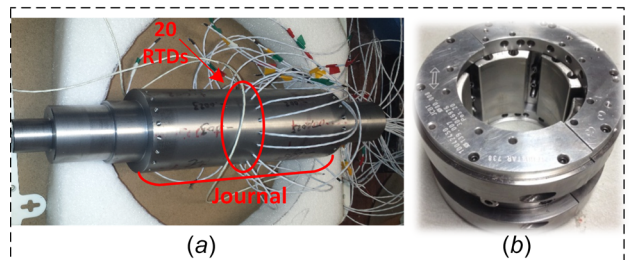
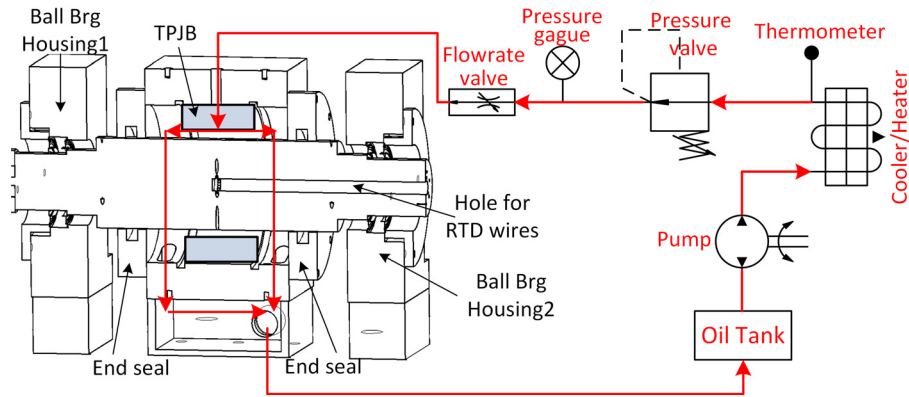


Fig. 2 (a) Shaft with eccentric journal and 20 internally routed RTDs and (b) TPJB test bearing



**Fig. 3 Key components of the TPJB-ME test rig hydraulic system**

**Table 1 Parameter values of the test rig**

Lubricant parameters		Bearing parameters	
Viscosity at 40 °C (Ns/m <sup>2</sup> )	0.044	Load type	Load on pad
Viscosity coefficients (1/°C)	0.04218	No. pads	5
Supply temperature (°C)	28 ± 3 (cool), 41 ± 3 (hot)	Radius of shaft (m)	0.040
Flow rate (L/min)	17 (≤ 3 krpm), 21 (> 3 krpm)	Radial bearing clearance (m)	1.40 × 10 <sup>-4</sup>
Reference temperature (°C)	40	Pad preload	0.42
Shaft parameters		Bearing length (m)	0.08
Shaft total length (m)	0.40	Pad arc length (deg)	56
Shaft total mass (kg)	9.25	Pivot	Rocker
Journal radius (m)	0.040	Pivot offset	50%
Journal length (m)	0.21	Tested eccentricity	0, 32% C <sub>b</sub>
Journal centerline offset (m)	6.86 × 10 <sup>-5</sup>	Tested attitude angle	0 deg, 5.8 deg
Thermal expansion coeff. (1/°C)	1.2 × 10 <sup>-5</sup>	Speed (rpm)	Up to 5500
Reference temperature (°C)	25	Thermal expansion coeff. (1/°C)	1.2 × 10 <sup>-5</sup>
Ball bearing stiffness (N/m)	1.6 × 8	Reference temperature (°C)	25

eccentric journal to execute a synchronous, circular orbit of radius  $r$  within the TPJB. This emulates the synchronous whirl that occurs in an operating machine under the influence of mass imbalance, and is the known source of asymmetric heating and consequent thermal bow in the Morton effect. The tolerance limitations on machining the eccentric journal result in an orbit radius  $r$  that exceeds the typical values observed in most machinery, so it might represent the case of a severe ME event. All RTDs are electrically isolated from the shaft with a thin thickness, highly thermally conductive epoxy and have wire leads that are routed via the hollow shaft to the slip ring at the nondrive end. The output wires of the slip ring transmit the signals to the data acquisition board over the operating speed (rpm) range. Orthogonally oriented noncontacting eddy current sensors are installed at both bearings yielding “X1, Y1, X2, and Y2” relative shaft displacement signals, and a fifth eddy current sensors is installed to provide a tachometer (key-phaser) output signal. The high combined stiffness of the ball bearings and their rigid support structures elevate the 1st critical speed above 40,000 rpm, which assures that support motion is minimal at the max operating speed 5500 rpm of the test rig. The lateral position of the TPJB centerline with respect to the shaft (ball bearings) centerline can be adjusted utilizing jack-bolt set screws that translate the TPJB to achieve the desired static eccentricity and attitude angle. The two tested operating eccentricities are  $e_1 = 0$  and  $e_2 = 32\%C_b$ , and the corresponding attitude angle is held close to zero, to simulate typical TPJB operation.

Figure 3 illustrates key components in the TPJB-ME test rig’s hydraulic system. The TPJB’s VG 46 viscosity grade lubricant is routed from the supply tank through the pump and heater and into the oil inlet port on the top of the TPJB housing. The TPJB has a

directed lubrication nozzle system that sprays oil into the gaps at the leading edges of all pads. Two end seals restrict oil leakage from the bearing house to atmosphere, assuring that nearly all of the oil returns to the oil supply tank. The “oil supply” temperature of the lubricant entering the TPJB is controlled by an inline heater/cooler system, and the shaft speed is controlled with a VFD 25 hp electric motor. The bearing clearance, eccentricity, rotor speed, oil flow rate, and supply temperature are selected at the design stage to prevent overheating, oil starvation, and rubbing between the bearing and journal. Table 1 provides a summary of the parameter values for the test rig.

**2.2 Measured Shaft Temperature Distribution.** The RTD accuracy is 0.15 °C and the thermal response time is less than 1 s. Due to the high accuracy of the data acquisition system, the entire measurement error is mostly determined by the RTDs. All RTDs were calibrated at room temperature before each experiment to eliminate static output (drift) error. The oil supply temperature was set at 28 °C or 41 °C for cool and hot oil testing, respectively. Real-time recording of supply temperature indicated fluctuations within ±3 °C during the test sequence. All test conditions were repeated at least three times, and satisfactory repeatability was found with the journal  $\Delta T$  variation typically within 0.2 °C. All RTDs were recorded at a sampling frequency of 0.6 Hz over a recording duration of 8 min at each speed to ensure convergence of measurements to their steady-state values. The samples within the last 10 s were averaged to represent the steady rotor temperature, which is discussed in this section. Two bearing static eccentricities were tested with  $e_1 = 0$  and  $e_2 = 0.32C_b$  and with the

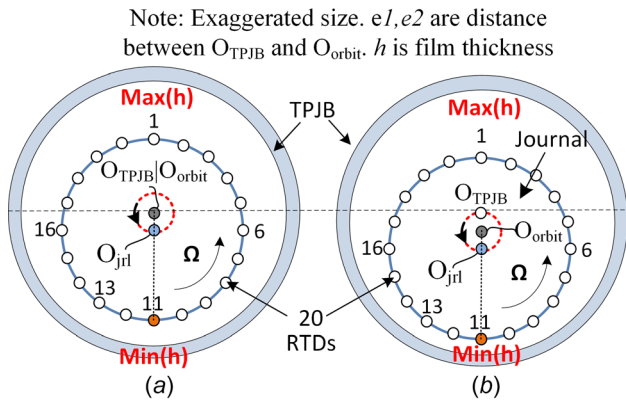


**Fig. 4 Cross-sectional view for both static eccentricities,  $e_1 = 0$  and  $e_2 = 0.32C_b$**

other variable values provided in Table 1. Figure 4 shows the cross section of the journal in the bearing for the two static eccentricity cases.

**2.2.1 Lower Temperature Supply Oil Test.** The journal orbit center  $O_{orbit}$  exactly coincides with the TPJB center  $O_{TPJB}$  when  $e_1 = 0$ , as shown in Fig. 4(a). RTD #11 experiences the minimum film thickness continuously during each synchronous whirl orbit and thus observes more viscous shearing than the other 19 sensors. In practice, the TPJB always operates with a static eccentricity to support the bearing loads, such as rotor weight and gear force. The operating eccentricity of the TPJB also changes with load,

speed, bearing configuration, etc., and can be as high as 80%  $C_b$  or even larger, especially for low speed and heavy loading conditions. The test eccentricity of  $e_2 = 32\%C_b$  was chosen to simulate a low to medium static bearing loading in practice and to avoid rubbing between the journal and the TPJB while considering the dynamic eccentricity caused by the eccentrically machined journal.

The journal orbit center  $O_{orbit}$  is displaced away from  $O_{TPJB}$  when the bearing is operating with a static eccentricity. In this case, RTD #11 experiences a fluctuating film thickness during its synchronous orbit, which might lead one to expect a reduction in the journal circumferential  $\Delta T$  compared with the centered case [8]. However, the film thickness at RTD #11 is smaller than the zero-eccentricity case when the journal center is at the lowest point in its orbit, leading one to expect a boost in the journal  $\Delta T$ . Test results with the two bearing eccentricities  $e_1 = 0$  and  $e_2 = 0.32C_b$ , and the lower supply oil temperature  $28 \pm 3^\circ\text{C}$  is presented in Fig. 5.  $\max(T)$  is the maximum journal temperature relative to the supply oil temperature, and  $\max(\Delta T)$  is the peak-peak temperature difference among all 20 RTDs in this figure. Note that all measurements in this paper are presented relative to the supply oil temperature, i.e.,  $T = 0$  corresponds to the given supply oil temperature.

The journal orbit size and shape may vary significantly with rotor speed, mechanical imbalance, bearing loads, etc., in an actual operating machine, making it difficult to conduct a single variable sensitivity study related to the ME. In contrast, the test rig facilitates ME sensitivity studies by maintaining an invariant journal orbit determined solely by the machined eccentricity of the journal centerline relative to the shaft, which is supported by relatively rigid ball bearings. This enables the study of static

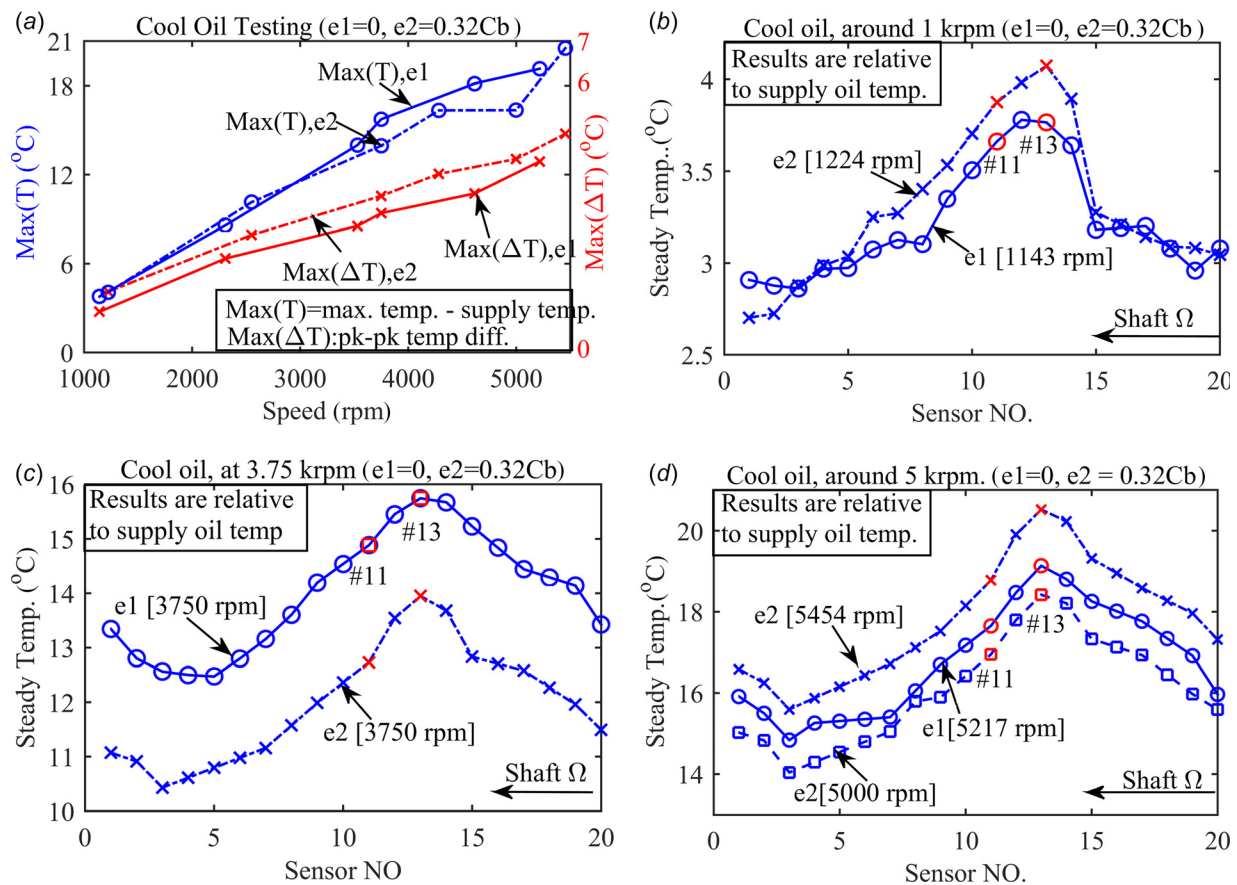


**Fig. 5 Measured rotor temperature with lower (cool) supply oil temperature and two static eccentricities: (a) maximum rotor temperature and peak-peak temperature difference, (b) rotor temperature profiles at approximately 1 krpm, (c) 3.75 krpm, and (d) 5 krpm**

eccentricity effects on ME while maintaining an invariant synchronous whirl orbit. Figure 5(a) shows that both  $\max(T)$  and  $\max(\Delta T)$  increase almost linearly with speed, and for every 1 krpm increment, the  $\max(T)$  and  $\max(\Delta T)$  grow by approximately  $3.8^\circ\text{C}$  and  $0.83^\circ\text{C}$ , respectively. Changing the bearing static eccentricity from 0 to  $0.32C_b$  does not significantly affect  $\max(T)$  but increases  $\max(\Delta T)$  by  $0.5^\circ\text{C}$  throughout the test speed range. The larger  $\max(\Delta T)$  indicates that the smaller minimum film thickness experienced by the high spot for the statically eccentric case (journal at the bottom of the orbit in Fig. 4(b)) intensifies the viscous shearing and journal asymmetric heating compared with the zero-eccentricity case, which results in a higher temperature difference around the journal. This trend in the measured  $\max(\Delta T)$  differs from that opined in Balbahadur and Kirk [8] that a centered orbit was more prone to the ME than an off-centered orbit. On the other hand, the measured trend is somewhat substantiated by Schmied et al. [20], where he mentioned that the ME was also observed in highly loaded bearings with the elliptical, off-centered journal orbits. The measured results indicate that one should not expect that increasing the static eccentricity will always improve suppression of the ME by reducing the journal  $\Delta T$ . Figures 5(b)–5(d) illustrate the steady journal temperature distribution at different speeds from all 20 RTDs. The temperature profiles are quite sinusoidal with the sensors close to the high spot, i.e., RTD #11, experiencing higher temperature. Interestingly, the hot spot does not exactly coincide with the high spot, which experiences the minimum film thickness. Instead, the hot spot is close to RTD #13 and lags the high spot by a certain angle, which is speed dependent and increases from 20 deg at 1143 rpm to 40 deg at 5454 rpm.

A simple linear interpolation method is employed to approximate the hot spot location, assuming that in most cases the hot spot is close to RTD #13, as depicted in Fig. 6(a). The three cases that may occur are: (1) the temperature of RTD #12 is lower than RTD #14, i.e.,  $T_{12} < T_{14}$ , then the hot spot will be at the crossing point between #13 and #14 and is located by extending two

adjacent sensor readings to locate the crossing point CP. The CP is always greater than  $T_{13}$  in the measured data. (2) if  $T_{12} = T_{14}$ , #13 is the hot spot; (3) if  $T_{12} > T_{14}$ , the hot spot will be at the CP between #12 and #13. The CP is always greater than  $T_{13}$  in the measured data.

The measured phase lag of the hot spot behind the high spot is shown versus speed in Fig. 6(b). Note that at low speed, the phase lag falls below 30 deg for both eccentricity cases and grows with speed and converges to 40 deg at 5454 rpm. Predicted phase lag for speeds greater than the measurement limit 5454 rpm indicates a reduced rate of growth of phase lag with speed. The measured phase lag differs from de Jongh's experiment [9], where the journal temperature distribution was estimated using only four sensors and the phase lag ranged from 15 deg at 4 krpm to 20 deg at 10.5 krpm. The difference may be due to the fewer number of sensors in de Jongh's experiment or due to the phase lag being sensitive to running speed and bearing configuration, which would dispel the notion of a nearly universal phase lag for the Morton effect. The current measurements are more consistent with Gomiciaga and Keogh's prediction [21], which was about 35 deg using a computational fluid dynamics model.

**2.2.2 Testing With Hot Supply Oil.** The supply oil temperature was increased from  $28^\circ\text{C}$  to  $41^\circ\text{C}$  and the related measurements are presented in Fig. 7. In Fig. 7(a), both the journal  $\max(T)$  and  $\max(\Delta T)$  increase monotonically with speed, which is similar to the cool oil case but is lower in magnitude. The eccentricity's influence on  $\max(T)$  is more evident than the cool oil case, and changing the bearing eccentricity from 0 to  $0.32C_b$  increases the journal  $\max(T)$  by  $2^\circ\text{C}$  on average. The journal  $\max(\Delta T)$  with  $e_2 = 0.32C_b$  is higher than  $e_1 = 0$  by  $0.5^\circ\text{C}$ , which is quite similar to the cool oil testing, indicating that increasing the bearing operating eccentricity may not mitigate the ME. Figure 7(b) shows that the phase lag between the high and hot spot grows from below 30 deg at low-speed to 40 deg at high-speed and almost levels off afterward, which is also similar to the cold oil case. Figures 7(c)–7(e) illustrate the circumferential journal temperature distribution versus speed, indicating that the hot spot near RTD #13 clearly lags the high spot RTD #11, which experiences the minimum film thickness. The cold spot is close to RTD #3, which is out of phase with the hot spot, indicating that the temperature profile is nearly sinusoidal.

The  $\max(T)$  and  $\max(\Delta T)$  for the hot oil testing are both lower than the cold oil case, and the ratio of the hot oil divided by the cool oil measurements is shown in Fig. 8. Note that the  $\max(T)$  is presented relative to the supply oil temperature, and thus smaller  $\max(T)$  for the hot oil does not indicate that the absolute temperature is lower. As shown in Fig. 8(a), the journal  $\max(T)$  with hot oil decreases for both eccentricity cases compared with the cool oil testing. The reduction percentage is 20–40% for  $e_2 = 0.32C_b$  and 40–60% for  $e_1 = 0$ , which is related to the reduction of lubricant viscosity, which drops by 43% compared to the cool oil at  $28^\circ\text{C}$ , as shown in Fig. 8(b). The reduction of the journal  $\max(\Delta T)$  is less significant and stays around 20% for all speeds as shown in Fig. 8(a). The viscosity–temperature profile is measured and curve fitted by an exponential function in Fig. 8(b), and the parameters are included in Table 1 and employed in the simulations in Secs. 4 and 5.

### 3 Simulation Introduction

Prediction of the ME involves sophisticated analysis of the rotor and bearing dynamics, heat transfer, and elastic and thermal deformation. The ME prediction differs from conventional thermo-elasto-hydro-dynamic analysis by focusing on the detailed journal temperature distribution, which is crucial in solving the thermal rotor bending and the rotor-bearing dynamic response. Palazzolo and co-workers [13–15] adopted a 3D FEM method to analyze the temperature distribution in the circumferential, radial, and axial directions of the lubricant film, bearing, and shaft. The

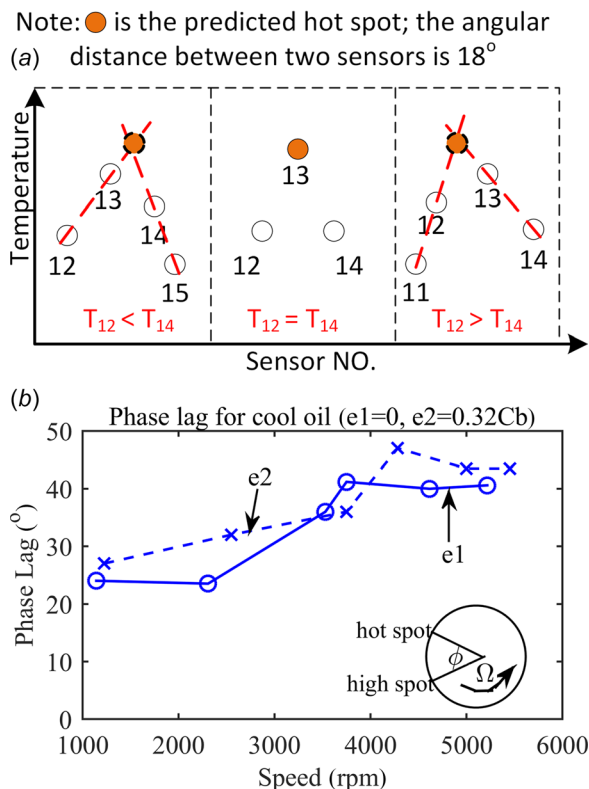
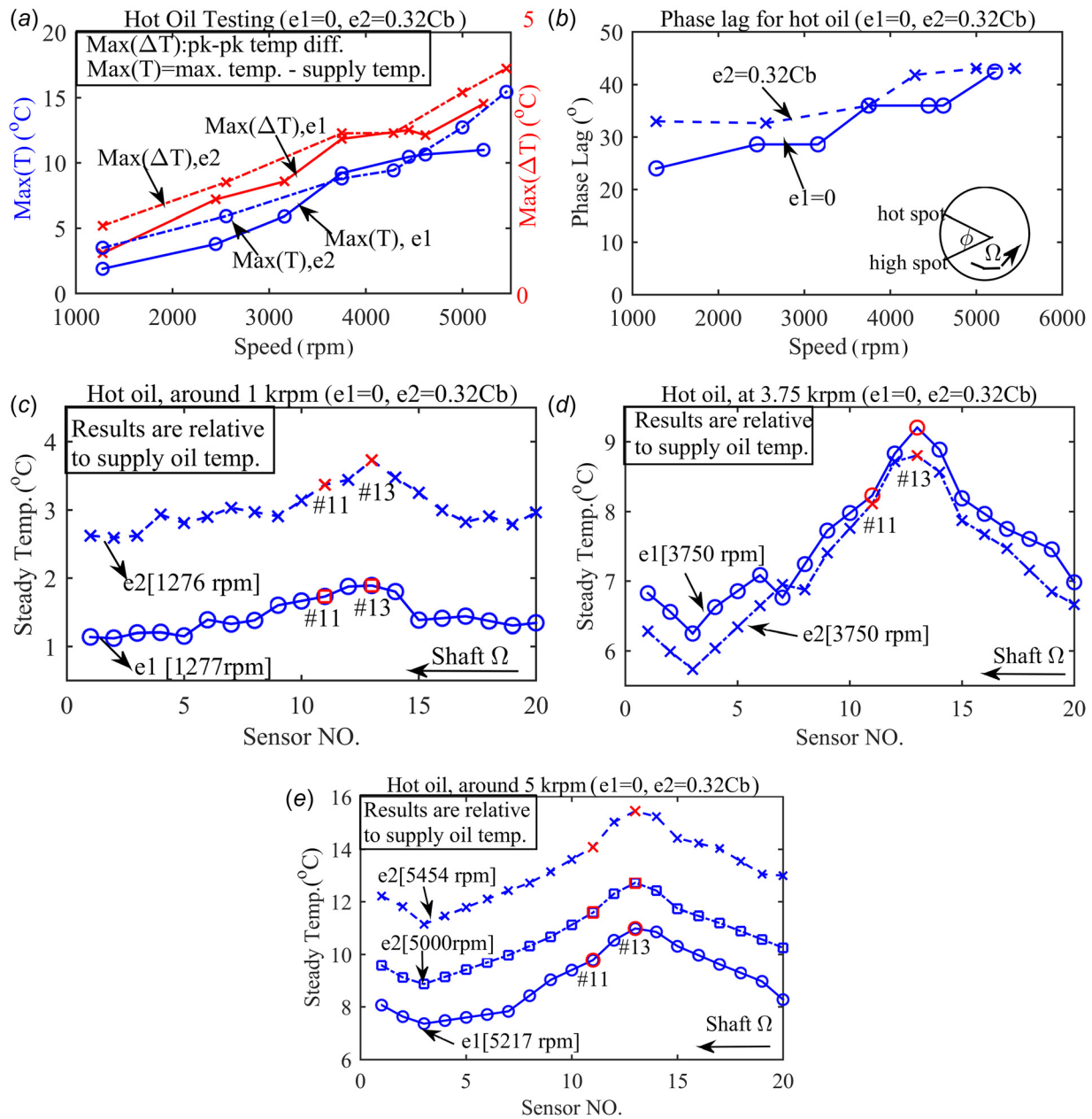


Fig. 6 (a) Linear interpolation to estimate hot spot location and (b) measured phase lag between the high spot and hot spot with cool supply oil and two eccentricities



**Fig. 7 Measured rotor temperature with hot supply oil and two eccentricities: (a) maximum journal temperature and peak–peak temperature difference, (b) phase lag between high spot and hot spot, (c) steady rotor temperature profile around 1 krpm, (d) 3.75 krpm, and (e) 5 krpm**

thermal deformation of the shaft and bearing is then calculated with 3D FEM, and then the bowed rotor profile is fed back into the dynamic solver together with the updated asymmetric hot bearing clearance to predict the rotordynamic response of the shaft assembly. The rotordynamics solver and temperature solver numerically integrate the governing equations successively to plot the rotor vibration and temperature versus time. Vibration response has a very short time constant relative to thermal response; therefore, the integration time span for the thermal solver is set to be longer than the dynamics solver to improve the computational efficiency with negligible loss in accuracy. Pad flexibility and pivot deformation can also be included in the model to improve prediction accuracy. ME prediction theory is developed below and compared with measurements from Sec. 2.

**3.1 Coupled Film Temperature and Pressure.** The ME is caused by the uneven oil viscous shearing around the journal and

can be significantly affected by the oil temperature due to the sensitive oil viscosity–temperature relationship, which is modeled by  $\mu = \mu_{ref} \exp(\alpha(T_{ref} - T))$  and illustrated in Fig. 8(b) with parameters in Table 1. The film temperature must be accurately predicted to update the local viscosity in the film with time. The 3D transient energy equation is solved with the FEM to provide a detailed film temperature distribution that varies with time. The velocity field required in the energy equation is obtained by solving the Reynolds equation with the FEM, utilizing the viscosity distribution, which is updated using the temperatures obtained by solving the energy equation. This coupled relationship requires that both the Reynolds (pressure, velocity) and energy (temperature) be solved simultaneously, which is performed by dividing the journal orbit into many steps and solving both equations successively within each segment [22]. Previous research utilized the simplified two-dimensional energy equation [16] by neglecting the axial film temperature variation, which was proven to overestimate the ME in certain cases [13].

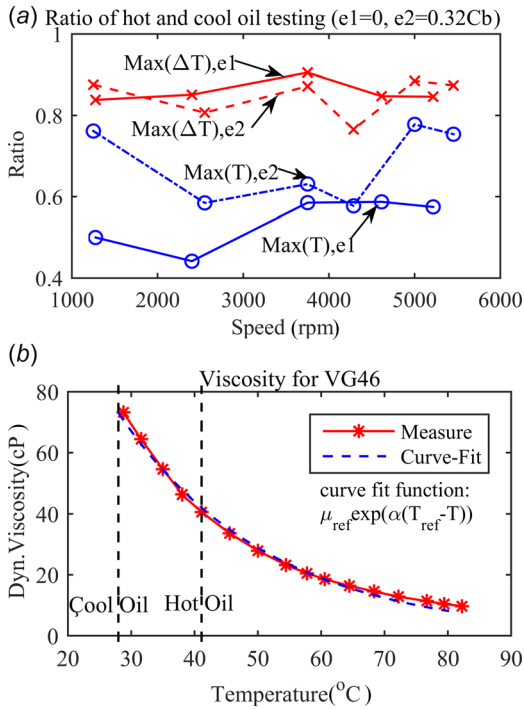


**Fig. 8 (a) Ratio between hot and cool oil testing and (b) oil viscosity profile versus different temperature**

The governing equation for the film pressure  $P$  is the Reynolds equation, which is derived from the continuity and momentum equation assuming that the fluid is Newtonian and the inertia and body force are neglected. The Reynolds equation with variable viscosity is shown in Eq. (1), where the bearing is stationary and the shaft is rotating with surface speed  $U = [\omega R, 0]$  in the tangential and axial direction, respectively,

$$\nabla \cdot (D_1 \nabla P) + \nabla D_2 \cdot U + \partial h / \partial t = 0 \quad (1)$$

where

$$D_1 = \int_0^h \int_0^y f_{\xi} d\xi dy - D_2 \int_0^h f_{\xi} d\xi, D_2 = \frac{\int_0^h \int_0^y f_1 d\xi dy}{\int_0^h f_1 d\xi},$$

$$f_{\xi} = \xi / \mu, f_1 = 1 / \mu$$

The oil viscosity  $\mu$  in Eq. (1) is highly temperature dependent and is obtained by solving the 3D energy equation in Eq. (2), where  $u$  and  $w$  are the oil velocity components in the circumferential and axial direction, respectively,  $\rho$  is the lubricant density,  $c$  is the heat capacity,  $k$  is the heat conductivity, and  $x, y,$  and  $z$  are the circumferential, cross-film, and axial direction, respectively,

$$\rho c \left( \frac{\partial T}{\partial t} + u \frac{\partial T}{\partial x} + w \frac{\partial T}{\partial z} \right) = k \left( \frac{\partial^2 T}{\partial x^2} + \frac{\partial^2 T}{\partial y^2} + \frac{\partial^2 T}{\partial z^2} \right) + \mu \left[ \left( \frac{\partial u}{\partial y} \right)^2 + \left( \frac{\partial w}{\partial y} \right)^2 \right] \quad (2)$$

The  $\partial T / \partial t$  term in Eq. (2) is usually neglected in conventional bearing analysis for bearing dynamic coefficient prediction, which assumes steady-state film temperature [23] conditions for infinitesimally small motions. The  $\partial T / \partial t$  term plays an important role in ME synchronous instability analysis since the orbit is finite causing the film thickness and ensuing shear-induced internal heat generation to change throughout the orbit period. The thermal

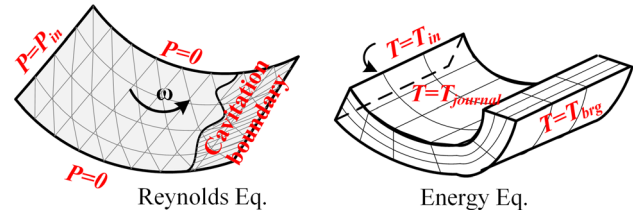


**Fig. 9 Boundary conditions for the Reynolds and Energy equations solution [14]**

time constant of the film can be comparable to the rotor revolution period, indicating that the film temperature change may lag the film thickness change, affecting the rotor circumferential temperature distribution. A quadratic up-winding scheme [24] is utilized in the FEM solution to suppress the numerically induced spatial oscillations caused by the convection term on the left side of Eq. (2). Note that most simplified ME analyses solve the steady-state energy equation and thus cannot predict the exact hot spot position relative to the high spot.

Figure 9 shows the boundary conditions used in solving the film pressure and temperature equations. The Reynolds boundary conditions of zero pressure and normal pressure gradient at the cavitation boundary are enforced in solving the Reynolds equation.

The energy equation boundary conditions include: (a) the temperatures at the inner and outer surfaces of the film are set equal to the journal and bearing surface temperatures and (b) the inlet temperature along the pad leading edge is calculated using mixing theory [13,25,26], which accounts for most of the hot oil being carried over from the previous pad trailing edge to the next pad leading edge. The mixing temperature formula employed in the current research is shown in Eq. (3), where  $\lambda$  is the mixing coefficient,  $Q$  is the flow rate,  $T$  is the film temperature, and the superscript indicates the pad number. For the present prediction,  $\lambda = 0.8$ , which indicates that 80% of the inlet oil is assumed to be carried over from the previous pad trailing edge and the balance is supplied by fresh oil. If  $Q_{out}^{i-1} < \lambda Q_{in}^i$ , all hot oil from the previous pad trailing edge is assumed to be carried over to the next pad. The parameter  $\lambda$  is estimated by correlating the simulation predictions with measured flowrates and shaft temperatures

$$T_{in} = \begin{cases} \frac{Q_{out}^{i-1} T_{out}^{i-1} + [Q_{in}^i - Q_{out}^{i-1}] T_{supply}}{Q_{in}^i} & \text{if } Q_{out}^{i-1} < \lambda Q_{in}^i \\ \frac{\lambda Q_{in}^i T_{out}^{i-1} + [Q_{in}^i - \lambda Q_{in}^i] T_{supply}}{Q_{in}^i} & \text{if } Q_{out}^{i-1} \geq \lambda Q_{in}^i \end{cases} \quad (3)$$

**3.2 Dynamic Model.** The ME is commonly observed in overhung rotating machinery, where rotor thermal bending at a journal may add significant thermally induced, effective mass imbalance at the overhung node. The aim of the test rig is limited to investigating the asymmetric journal temperature distribution as opposed to reproducing a full blown ME occurrence. Thus, the rig uses a short rigid, synchronously whirling rotor without an overhung mass. The ball bearings react with the rotor-induced loading while restricting its lateral motion, and thus the journal orbit remains nearly invariant under all operating conditions. The mechanical imbalance  $\bar{m}\bar{e}$  due to the intentionally machined eccentric journal and the hydrodynamic forces at the TPJB location both affect the rotor response in the rig. The rotor is connected to the drive motor with a very flexible coupling that has negligible influence on the rotor motion or bearing forces. The rotor equations of motion are given in Eq. (4), where  $m$  is the rotor mass,  $k$  is the ball bearing stiffness,  $w$  is the rotor weight, and  $F_x$  and  $F_y$  are the hydrodynamic forces from the TPJB. Note that  $x$  and  $y$  locate the shaft geometrical center, i.e., the center of the journal orbit, which differs from the journal center by the machined eccentricity  $r = 0.0027$  in

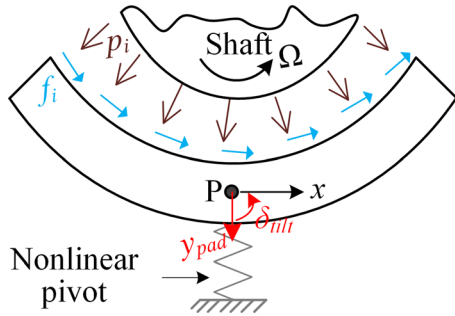


Fig. 10 Journal and rigid pad force diagram

$$\begin{bmatrix} m & 0 \\ 0 & m \end{bmatrix} \begin{bmatrix} \ddot{x} \\ \ddot{y} \end{bmatrix} + \begin{bmatrix} 2k & 0 \\ 0 & 2k \end{bmatrix} \begin{bmatrix} x \\ y \end{bmatrix} = \overline{m} \omega^2 \begin{bmatrix} \cos(\omega t) \\ \sin(\omega t) \end{bmatrix} + \begin{bmatrix} 0 \\ -w \end{bmatrix} + \begin{bmatrix} F_x \\ F_y \end{bmatrix} \quad (4)$$

The test bearing is a five-pad load-on-pad TPJB with a cylindrical pivot, 50% offset, and pad thickness of 11 mm. As shown in Fig. 10, the simulation model permits tilt  $\delta_{\text{tilt}}$  and translation  $y_{\text{pad}}$  of each pad about its pivot, and the individual pivot deformation and stiffness are predicted based on Hertzian contact theory [27]. Pad flexibility [14] was initially included in the model using 3D FEM; however, the results were quite similar to the rigid pad model indicating that the rigid pad model was sufficiently accurate for all ensuing simulations. The governing equations for the  $i$ th rigid pad shown in Fig. 10 are given in Eq. (5), where  $m_{\text{pad}}$  and  $I_{\text{pad}}$  are the pad mass and moment of inertia,  $p_i$  and  $f_i$  represent the nodal hydrodynamic and viscous forces,  $p_{iy}$  and  $f_{iy}$  are the  $y$  components of  $p_i$  and  $f_i$ , and  $M_{pi}$  and  $M_{fi}$  are the moments about the pivot  $P$  caused by nodal forces  $p_i$  and  $f_i$

$$\begin{cases} m_{\text{pad}} \ddot{y}_{\text{pad}} = -k_{\text{pvt}} y_{\text{pad}} + \sum p_{iy} + \sum f_{iy} \\ I_{\text{pad}} \ddot{\delta}_{\text{tilt}} = \sum M_{pi} + \sum M_{fi} \end{cases} \quad (5)$$

**3.3 Thermal Model.** The accurate prediction of rotor and bearing temperatures is important from a rotordynamic perspective for at least two reasons. First, the temperature rise may cause thermal expansion, reducing the operating bearing clearance, which affects the bearing stiffness and damping. Second, in overhung machines, the  $\Delta T$  across the journal circumference may bend the shaft and cause thermal imbalance and the ME. The test rig is designed to study the source of these responses, namely, the asymmetric temperatures induced on the journal by rotor spinning and synchronous whirling. The 3D heat conduction equation applies to modeling both the rotor and the bearing pads and is solved with the FEM using 3D, eight-node iso-parametric solid elements. The conduction equation is

$$\frac{\partial^2 T}{\partial x^2} + \frac{\partial^2 T}{\partial y^2} + \frac{\partial^2 T}{\partial z^2} = \frac{\rho c}{k} \frac{\partial T}{\partial t} \quad (6)$$

where  $k$  is the heat conductivity,  $\rho$  is the density, and  $c$  is the heat capacity. The lubricant (Eq. (2)) and rotor and pad (Eq. (6)) thermal problems are solved as a coupled system with both internal and external boundary conditions. The internal boundary conditions include continuity of temperature and heat flux on the lubricant\journal and lubricant\pad surfaces. The lubricant\journal boundary condition is imposed considering that the shaft is spinning with speed  $\omega$ , so  $\theta$  in the rotor rotational frame corresponds to  $(\theta + \omega t)$  in the lubricant fixed frame. The shaft and pad

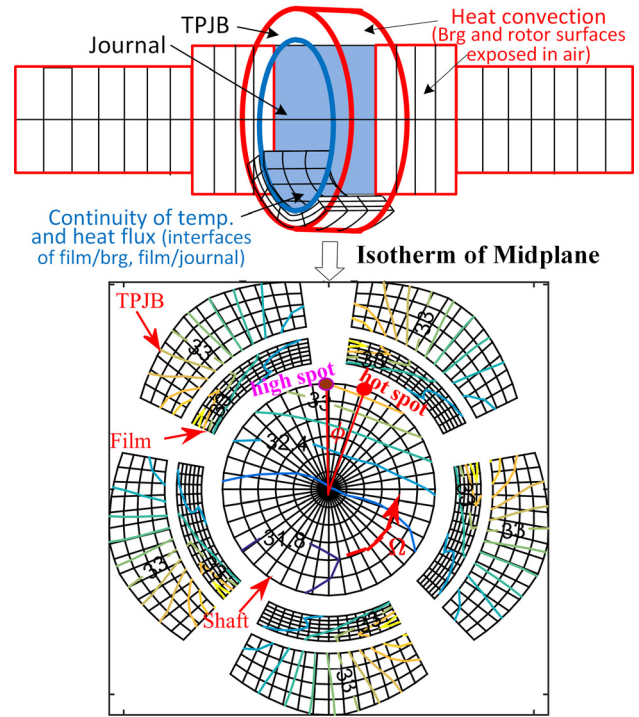


Fig. 11 Boundary conditions for the coupled journal/shaft/film/pad thermal model

surfaces exposed to air have a heat convection boundary condition  $q = \bar{h}(T - T^\infty)$ , where  $q$  is the heat flux,  $T^\infty$  is the ambient temperature, and  $\bar{h}$  is the heat convection coefficient.  $T^\infty$  is set to 30 °C for all simulations and  $\bar{h}$  is set to the constant value 10 W/m<sup>2</sup> °C. The latter was justified by varying  $\bar{h}$  and finding that the resulting changes in the predicted rotor temperature varied by less than 1 °C. Figure 11 illustrates the thermal boundary conditions and the cross section temperature distribution for identifying the hot spot position. The thermal and vibrations problems are solved in a staggered manner for computational efficiency [15] so that the thermal solution is updated after the vibrations have reached steady-state and vice versa.

The thermally induced deformation of the shaft, journal, and pads is modeled with a 3D solid, structural FEM model, sharing the same nodes as the 3D solid, thermal FEM model. The temperature solver calculates all nodal temperatures of the rotor and bearing forming the thermal load vector, which is applied to calculate thermally induced deformations. The hot bearing clearance and the film thickness distributions are then updated using these deformations. The test rig is designed to only measure the asymmetric journal temperature distribution and lacks an overhung mass, which is needed for the synchronous instability response of the ME. For the more general case in modeling actual overhung machines, the shaft thermal bow also needs to be calculated and fed back to the rotordynamic solver to predict the transient dynamics of the rotor and bearing in the next integration cycle. In this case, the transient numerical integration of the temperature and dynamic solvers are coupled and successively solved in the time domain until convergence is achieved. The rotor speed is set to a constant value for predicting the steady-state rotor and bearing temperatures and dynamics. Details of the ME simulation algorithm can be found in Ref. [14] and are not repeated in this paper.

## 4 Simulation Results Using a High-Fidelity, Transient Modeling Approach

**4.1 Comparison of Simulation and Experimental Results.** Figure 12 shows both prediction (dashed) and test (solid)

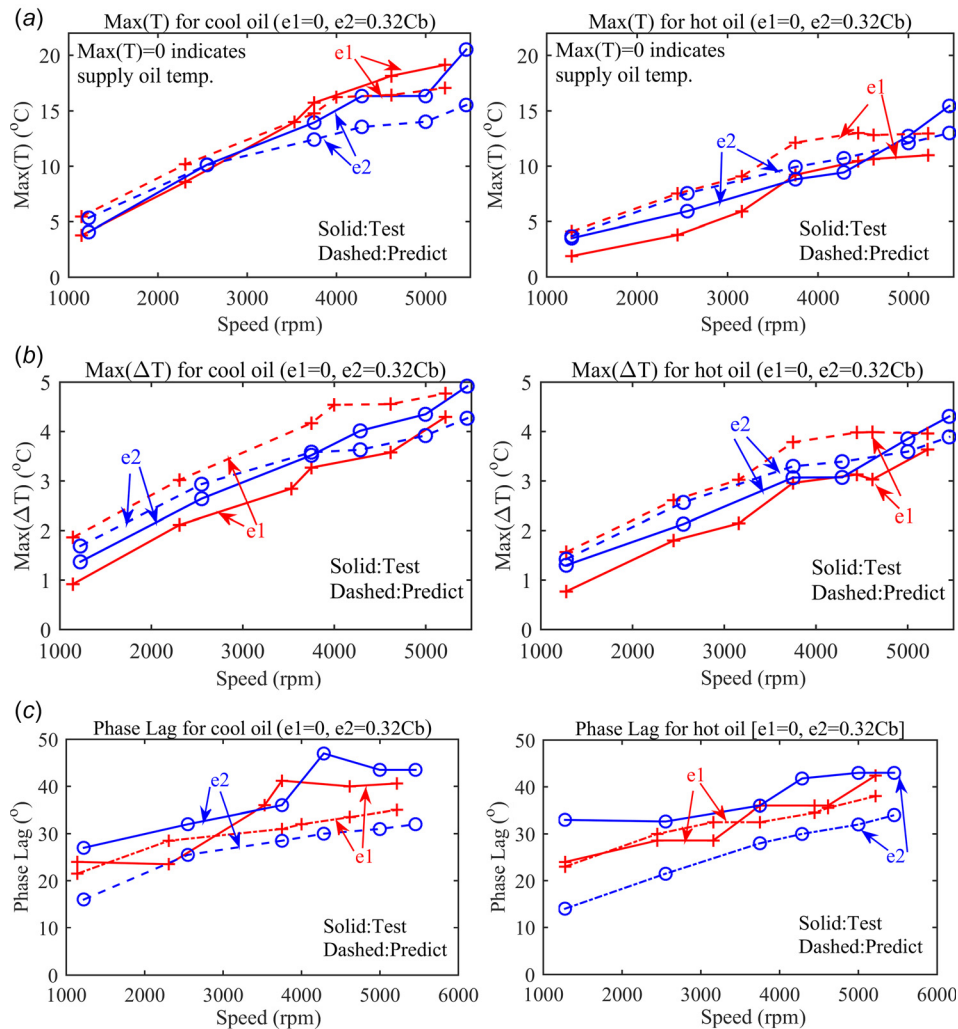


**Fig. 12** Experimental and predicted journal temperature comparison for cool and hot oil cases: (a) maximum temperature, (b) peak–peak temperature difference, and (c) phase lag between high and hot spot

temperatures. The average difference for  $\max(T)$  between prediction and experiment over the speed range and with the two bearing eccentricities and two oil supply temperatures is about  $1.9^\circ\text{C}$ . Similarly, the difference for  $\max(\Delta T)$  is  $0.6^\circ\text{C}$ , indicating that the prediction accuracy is quite satisfactory. The simulation for  $e_1 = 0$  with both cool and hot supply oil in Fig. 12(b) overpredicts  $\max(\Delta T)$ , while the prediction for  $e_2 = 0.32C_b$  has better agreement with the test measurements. The phase lag between the journal high and hot spots shown in Fig. 12(c) indicates a generally lower prediction value relative to the measurement. The current test rig, by far, has the most sensors for measuring the ME in the public domain, and yet still only has a resolution of  $18^\circ$ , i.e.,  $360^\circ/\text{Sensor\_NO}$ . The trend of the measured and predicted phase lag versus speed is in general agreement and the difference between the measured and predicted values typically falls within 10 degrees and even less for the centered journal case. Given the coarse resolution of the measurements, this is considered a reasonable difference supporting the accuracy of the predictions. The phase lag can be explained as follows: Assume that at some instant in time within the orbit,  $t = t_0$ , the film thickness reaches its minimum value at the “high spot” angular position  $\theta = \theta_0$ . The shearing (heat generation) in the viscous oil reaches its maximum value at  $\theta = \theta_0$ . The thermal mass ( $mC_p$ ) causes a time delay in the resulting peak temperatures to occur in the lubricant and rotor. The rotor is rotating during this delay, which causes the peak temperature to occur at an angular hot spot location displaced from

the high spot by the Morton effect “lag” angle. Simulations performed at speeds above the max test speed of 5454 rpm, which resulted from power and oil flow limits, indicate that the phase lag converges to about  $40^\circ$  as speed is increased. Some possible reasons for the differences between prediction and experiment are (1) spatial resolution of the measurement, (2) the measurement tolerance of the bearing clearance and ball bearing stiffness, and (3) the simplified mixing coefficient model. Eighty percent of the inlet flow for each pad is assumed to be carried over from the previous pad’s trailing edge and mixing together with 20% fresh supply oil, for all predictions. The mixing coefficient is estimated based on the measured flow rate and journal temperature. The actual mixing process is quite complex and is reported to change with rotor speed and bearing eccentricity.

The component mesh sizes were selected to balance computational cost and accuracy and were: rotor 3D model ( $40 \times 16 \times 7$ ), each pad ( $15 \times 6 \times 5$ ), and the film for each pad ( $15 \times 6 \times 6$ ) in the circumferential, axial, and radial directions. The wall clock time required to complete one rotating speed case in Fig. 12 with converged rotor  $\Delta T$  was approximately 2 h with the current mesh size.

**4.2 Parametric Studies of Bearing Clearance and Mixing Coefficient.** Bearing radial clearance  $C_b$  has been reported to affect the ME instability by changing the lubricant viscous shear

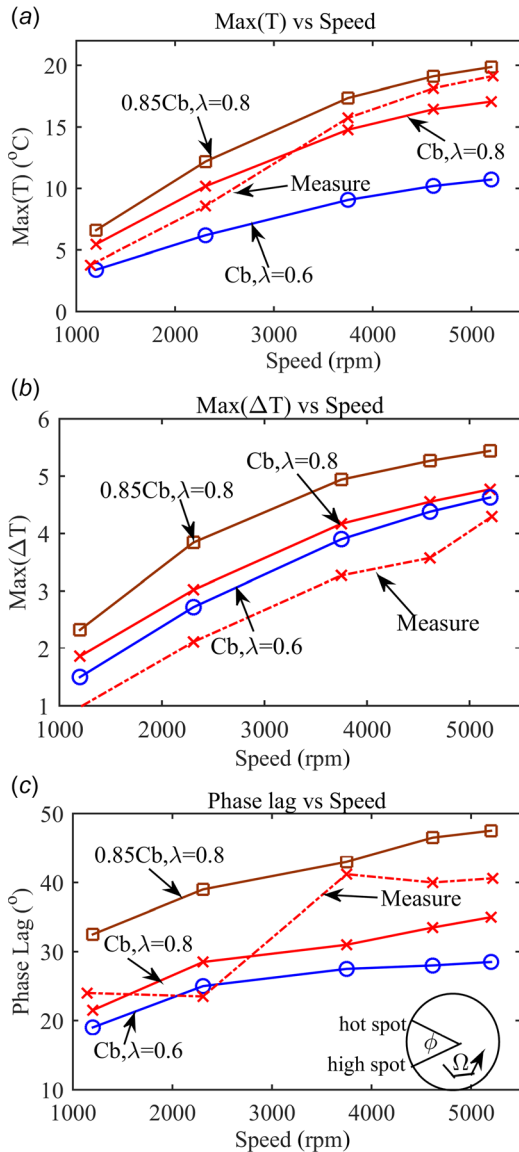


**Fig. 13 Parametric studies of bearing clearance and mixing coefficient by predicting (a) maximum journal temperature, (b) peak-peak temperature difference on journal circumference, and (c) phase lag between high and hot spot**

stresses. In 1998, de Jongh and Van Der Hoeven [28] increased the  $C_b$  from 0.19% to 0.22% (ratio defined as  $C_b/R_{brg}$ ) to successfully suppress an ME event. In 1997, Corcoran et al. [29] reduced the  $C_b$  by 33% and found that although the rotor vibration was suppressed, overheating inside the bearing occurred. The mixing coefficient  $\lambda$  is another important parameter that affects the rotor, bearing, and oil temperatures and is likely to change the ME instability [30]. The recent direct bearing lubrication results using spray bars [31], inlet groove [32], etc. can reduce the carry-over flow ratio and thus cool the rotor and bearing. In this section, three different cases are simulated with (a)  $0.85C_b$  with  $\lambda=0.8$ , (b)  $C_b$  with  $\lambda=0.6$ , and (c)  $C_b$  with  $\lambda=0.8$ , where case c is consistent with the experimental condition and discussed in Sec. 4.1. Results are illustrated in Fig. 13 for the cold supply oil and zero static eccentricity case. Note that reducing  $C_b$  by 15% increases the  $\max(\Delta T)$  by 11%, indicating that the ME might become more severe. Reducing  $\lambda$  suppresses both the journal  $\max(T)$  and  $\max(\Delta T)$  although the reduction of  $\max(T)$  is more evident in this case. The influence of phase lag between the high spot and hot

spot is quite similar to  $\max(\Delta T)$ , indicating that the hot spot will be closer to the high spot with more direct lubrication and larger  $C_b$ .

## 5 Compare with Simplified Morton Effect Analysis

**5.1 Version 1 of the Simplified Method.** Murphy and Lorenz [12] proposed a faster, yet more approximate ME analysis for estimating rotordynamic, synchronous spiral stability with a frequency domain formulation. The relationships between synchronous vibration, imbalance, and journal  $\Delta T$  were assumed to be linear and expressed in terms of influence coefficients. In 2015, Panara et al. [18] modified Murphy's method to predict the measured journal  $\Delta T$  with an additional assumption on pad tilting angle to improve efficiency. This is discussed further in step 3 below. The present paper only considers the journal differential temperature  $\Delta T$  aspect of the overall ME phenomena. Thus, this is the only part of the Murphy and Lorenz' method considered for comparison.

*Step 1.* Run conventional bearing design software to get the static eccentricity, pad tilting angles, and bearing dynamic coefficients.

*Step 2.* Specify a journal orbit and divide it into dozens of discrete points.

*Step 3.* Run the same bearing program to obtain the film temperature profile around the journal with its center positioned at each of the orbit points; note that the pad tilting angles can be updated accordingly (Murphy's method [12]), or simply set to be the angles in step 1 with the journal positioned at the orbit center (Panara's method [18]).

*Step 4.* Average the temperature profiles from all orbit points to get the asymmetric shaft surface temperature, noting that the shaft also rotates as it whirls around the orbit.

This simplified steady method is intuitive to implement and can be quite fast compared with the current high-fidelity method, which requires the numerical integration for the coupled, transient response of vibration and temperature. Nevertheless, the simplified process is a tradeoff between execution speed and accuracy. The present high-fidelity method utilizes mainly 3D FEM component models, having minimal reliance on assumptions, which, to some degree, compromises the accuracy of the simplified method. These assumptions of the simplified method include:

- (1) The journal  $\Delta T$  is assumed to be proportional to vibration amplitude, which was proven to be inaccurate when the journal orbit size exceeded 20% of bearing clearance by Childs and Saha [33],
- (2) the actual rotor thermal bow due to the ME is assumed to act as a thermally induced mass imbalance, which neglects the bending moment and has been shown to yield an inaccurate instability onset speed by Tong et al. [15],
- (3) most commercial bearing codes assume an insulated rotor surface outside of the journal so that the influence from the rotor thermal boundary conditions is neglected. However, this assumption can compromise the accuracy of the ME prediction, which was shown to be quite sensitive to the rotor's heat exchange with its surroundings by Suh and Palazzolo [30], and
- (4) the ME is assumed to be only rotor speed dependent and not rotor acceleration dependent, which is inconsistent with several case studies where for instance, de Jongh mentioned that any speed increase of 1000 rpm within 10 s directly triggered the instability [28]; however, in Ref. [9], for another compressor, he found that by quickly raising the rotor speed, it was possible to run through the unstable speed range.

The most difficult yet important step in the simplified method is the prediction of journal  $\Delta T$ , where both the  $\Delta T$  magnitude and the hot spot position (phase lag relative to the high spot) are

important. An upgraded Murphy [12] ME analysis is developed here in order to improve the prediction of the journal  $\Delta T$ . The framework of the Murphy approach is retained yet modifications are adopted for accuracy improvement. The upgraded approach adopts a higher fidelity model when executing steps 1 and 3. And two options (Panara\* and Murphy\*) are provided to update the steady-state tilt angles and pivot deflections.

The results from the upgraded simplified approaches are compared with the high-fidelity approach in the results section. The (Version 1) upgraded Murphy method has the following features:

- (1) Utilize a 3D steady-state energy equation to account for the film temperature variation in the axial direction.
- (2) Solve for the 3D steady-state rotor and bearing temperature distribution with FEM including heat convection from the rotor external to the bearing.
- (3) Include bearing and rotor thermal expansion, which is used to update the hot bearing clearance.
- (4) Include pivot flexibility using Hertzian contact theory [27] to calculate the nonlinear pivot deflection.
- (5) The pad tilt angles and pivot displacements can be updated according to the journal orbit position (Murphy's method), or simply set to be the steady angles and displacements calculated with the journal fixed at the orbit center (Panara's method).

The predicted journal  $\max(\Delta T)$  for various static eccentricities and supply oil temperature is shown in Fig. 14. The phase lag prediction is not shown because the simplified approach neglects all transient process and thus always predicts zero phase lag, i.e., the hot spot coincides with the high spot. Murphy's approach [12] not only uses a constant 20 deg phase lag between the hot spot and the high spot in a case study but also points out that the angle could be between 0 deg and 60 deg. Figure 14 compares the test measurements of journal  $\max(\Delta T)$  with predictions from the "Transient" (high fidelity transient based), "Murphy\*," and "Panara\*" methods. The Murphy method updates the pad angles at each orbit point, and the Panara approach uses the pad angles that occur at the orbit center, for all orbit positions. It should be noted that the simplified approach results are obtained using a

high fidelity model including 3D thermal and deformation models and convective heat transfer on the shaft segments adjacent to the bearing. Most commercial codes utilize much simpler two-dimensional or even one-dimensional thermal models and neglect thermal and centrifugally induced deformations. Thus, we have implemented the simplified method with arguably the best available steady-state model, for the sake of a fair comparison. The simplified method predicts relatively accurate journal  $\max(\Delta T)$  at low speed. However, when the speed increases, both simplified methods Murphy\* and Panara\* deviate from the high-fidelity method and overpredict the  $\max(\Delta T)$  by almost 2 °C at 5454 rpm, while the high-fidelity method shows very good agreement with the experimental measurements. The Murphy\* method has a higher accuracy than the Panara\* method because the former updates the pad tilt angles and pivot displacements at each point on the journal orbit, making the film thickness and temperature predictions more accurate. The above observations are based on the experimental test configuration, which has a relatively larger bearing clearance compared with industry practice due to machining limitations of the eccentric journal. A second comparison among the three prediction methods, without test data, is presented in Sec. 5.2 utilizing a bearing clearance that is more representative of industrial practice.

The component mesh sizes utilized for the Panara\* and Murphy\* methods were the same as used in the transient method predictions in Sec. 4.1. The wall clock time for either of the steady methods to complete one rotating speed case in Fig. 14 was approximately 20–40 min. This is approximately 3–6 times faster compared with the transient method for the same mesh size. The above comparison includes only the determination of the journal  $\Delta T$ . This is only one part of the entire ME calculation, which also includes rotor thermal bow/imbalance deflection determination. Nevertheless, the thermal bow solver is generally much less time-consuming so that the journal  $\Delta T$  prediction is the main driver of computational cost.

**5.2 Version 2 of the Simplified Method.** The following assumptions contribute to the lower accuracy observed in the simplified approach results:

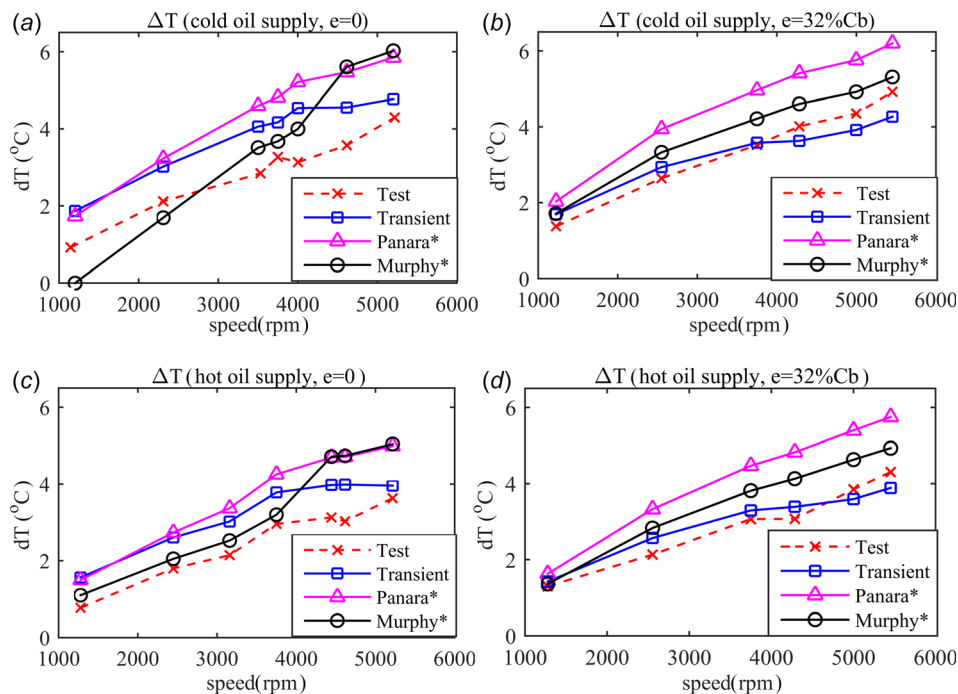


**Fig. 14 Predictions of journal temperature difference by the high-fidelity and simplified analysis (a) cold oil supply, eccentricity  $e = 0$ , (b) cold oil supply,  $e = 0.32C_b$ , (c) hot oil supply,  $e = 0$ , and (d) hot oil supply,  $e = 0.32C_b$**

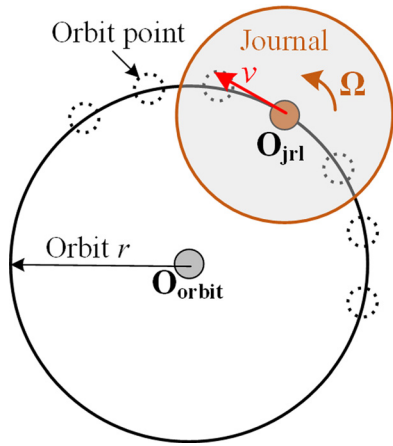


**Fig. 15 Journal center whirling along an orbit with velocity  $v$**

- (1) In the Panara\* method, the same tilt angles calculated with the journal at  $O_{orbit}$  are imposed on the bearing pads when the journal is displaced at all points on the synchronous whirl orbit in Fig. 15.
- (2) The shaft whirling velocity  $v$  along the orbit creates an additional source term in the Reynolds equation, which is neglected in the steady-state solution employed in the simplified approach. This influences the predictions of local pressures, velocities, and temperatures, and also pad tilt angles and film thickness.

A further refined variation of the Murphy simplified approach is proposed to provide increased accuracy while still requiring significantly less computational time relative to the high-fidelity transient approach.

Simplified approach—Version 2 differs from Version 1 in calculating updated pad tilt angles at each point along the orbit (i.e., abandon assumption 1), and including effects of the whirl velocity

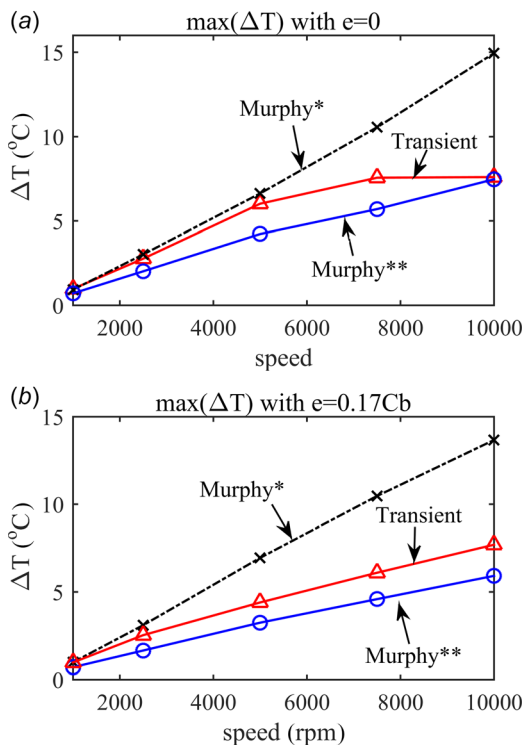


**Fig. 16 Predicted TPJB journal  $\Delta T$  for the simplified and high fidelity methods with reduced clearance: (a) eccentricity = 0 and (b) eccentricity =  $0.17C_b$**

$v$  in the Reynolds equation (i.e., abandon assumption 2). These alterations would most likely require minor code changes by a developer if a commercial bearing modeling code is employed. The Version 1 and Version 2 simplified method results are compared to each other and to the high-fidelity transient method results below. A smaller clearance is employed in the comparison to be more consistent with industrial practice. The TPJB clearance is reduced to 0.003 in (0.0762 mm,  $C_b/R_{shaft} = 0.19\%$ ) with a preload of 0.3, and the journal orbit radius is reduced to  $5E-4$  in (0.0127 mm). Figure 16 shows the predicted journal  $\max(\Delta T)$  for the cool supply oil and two eccentricity cases, i.e., zero and  $17\%C_b$ . The predictions are performed by the two simplified methods and the transient high-fidelity method, where Murphy\* and “Murphy\*\*” are the simplified Version 1 and Version 2. The phase lag plot is not shown because in the steady (simplified) analysis, the hot spot always coincides with the high spot. The Version 1 simplified method significantly overpredicts the journal  $\max(\Delta T)$ , while the Version 2 method predicts results that are in much better agreement, compared to the high-fidelity approach. Nevertheless, Version 2 is much slower than Version 1 because it needs to calculate the pad tilting angles along the journal orbit, which can be quite computational intensive for the case with multiple-pad TPJB and dozens of orbit points.

## 6 Summary and Conclusion

A test rig was developed utilizing 20 RTDs to measure the circumferential temperature distribution on a synchronously whirling journal. This provided a far greater resolution of the temperature distribution than prior work that employed at maximum 8 temperature sensors. In addition, the rig utilizes an eccentric journal and very stiff ball bearing supports, which produce a fixed orbit geometry independent of speed, and other operating condition changes. This facilitates the identification of the causalities between the temperature responses and operating condition changes without the influence of a simultaneously varying orbit. The operating conditions that were varied include two supply oil temperatures (28 °C and 41 °C), two bearing eccentricities (0 and  $32\%C_b$ ), and rotor speeds ranging from 0 to 5500 rpm. Test results for peak–peak journal  $\Delta T$  and maximum temperature were measured and compared with predictions obtained from a high-fidelity, 3D transient analysis and a simplified steady-state ME analysis developed by Murphy and Lorenz [12]. Hot spot lag angles were also estimated from the 20 RTD measurements and compared with only the high-fidelity model predictions, since the simplified, steady-state model was limited to predicting a zero phase lag angle under all conditions. A novel (Version 2) simplified model was derived by including the journal center’s orbit velocity in the Reynolds equation solution. The results show significantly improved agreement with the high fidelity, transient model predictions. Some specific conclusions from the study include:

- (1) The measured maximum journal temperature and peak–peak differential  $\Delta T$  increase nearly linearly with rotor speed under all conditions.
- (2) The measured journal temperature varies in a sinusoidal manner around the circumference. The hot spot is close to but lags the high spot and the cold spot is out of phase with the hot spot. The hot spot lags the high spot by an angle, which is speed dependent and increases from 20 deg at 1200 rpm to 40 deg at 5500 rpm and nearly levels off at high speeds.
- (3) The high-fidelity transient analysis predictions for journal  $\Delta T$  and hot spot position show good agreement with measurements.
- (4) Simulations demonstrate that the journal  $\Delta T$  is sensitive to the bearing clearance  $C_b$  and mixing coefficient  $\lambda$ . It was found that increasing  $C_b$  and reducing  $\lambda$  can reduce the

journal  $\Delta T$  and mitigate the ME under the condition of a constant journal orbit as in the test.

- (5) The simplified ME analysis by Murphy and Lorenz [12] is much faster than the transient, high-fidelity approach, but may predict significantly higher journal  $\Delta T$  than the experimental and high fidelity model results, and predicts a zero phase lag between the hot spot and high spot. An improved version of the simplified method including journal orbit velocity was developed and showed improved accuracy for journal  $\Delta T$  prediction relative to the original simplified approach.

Future work includes testing of other bearings, developing parameter selection rules to mitigate the ME, and experimentally investigating the influence of rotor backward whirl on the ME. This last topic will most likely include magnetic bearing actuators to produce the backward whirl orbits.

## Acknowledgment

The authors express their sincere appreciation to Mr. Erwin Thomas for providing excellent engineering skills in designing the temperature measurement system, Dr. John Kocur and the Exxon Mobil Corporation for providing the industrial tilt pad bearing, and the Texas A&M Turbomachinery Research Consortium for funding this research.

## Nomenclature

- $C_b$  = radial bearing clearance  
 $h$  = film thickness  
 $\max(T)$  = maximum temperature across the journal circumference relative to supply oil temperature  
 $\max(\Delta T)$  = peak–peak temperature difference across the journal circumference  
 $T_{\text{ref}}$  = reference temperature  
 $\Delta T$  = temperature difference across the journal circumference  
 $\lambda$  = mixing coefficient  
 $\mu$  = lubricant viscosity  
 $\mu_{\text{ref}}$  = viscosity at reference temperature  
 $\phi$  = phase lag between the hot spot and high spot

## References

- Fillon, M., Bligoud, J., and Frene, J., 1992, "Experimental Study of Tilting-Pad Journal Bearings—Comparison With Theoretical Thermoelastohydrodynamic Results," *ASME J. Tribol.*, **114**(3), pp. 579–587.
- Dowson, D., Hudson, J., Hunter, B., and March, C., 1966, "Paper 3: An Experimental Investigation of the Thermal Equilibrium of Steadily Loaded Journal Bearings," *Proc. Inst. Mech. Eng.*, **181**(2), pp. 70–80.
- Paranjpe, R., and Han, T., 1995, "A Transient Thermohydrodynamic Analysis Including Mass Conserving Cavitation for Dynamically Loaded Journal Bearings," *ASME J. Tribol.*, **117**(3), pp. 369–378.
- Knight, J., and Barrett, L., 1988, "Analysis of Tilting Pad Journal Bearings With Heat Transfer Effects," *ASME J. Tribol.*, **110**(1), pp. 128–133.
- Khonsari, M., and Beaman, J., 1986, "Thermohydrodynamic Analysis of Laminar Incompressible Journal Bearings," *ASLE Trans.*, **29**(2), pp. 141–150.
- Morton, P. G., 1975, "Some Aspects of Thermal Instability in Generators," G.E.C. Internal Report, Report No. S/W40 u183.
- Hesseborn, B., 1978, "Measurements of Temperature Unsymmetries in Bearing Journal Due to Vibration," Internal Report.
- Balbahadur, A. C., and Kirk, R., 2004, "Part I—Theoretical Model for a Synchronous Thermal Instability Operating in Overhung Rotors," *Int. J. Rotating Mach.*, **10**(6), pp. 469–475.
- de Jongh, F., and Morton, P. G., 1994, "The Synchronous Instability of a Compressor Rotor Due to Bearing Journal Differential Heating," *ASME Paper No. 94-GT-035*.
- Keogh, P., and Morton, P., 1993, "Journal Bearing Differential Heating Evaluation With Influence on Rotordynamic Behaviour," *Proc. R. Soc. London, Ser. A*, **441**(1913), pp. 527–548.
- Keogh, P., and Morton, P., 1994, "The Dynamic Nature of Rotor Thermal Bending Due to Unsteady Lubricant Shearing Within a Bearing," *Proc. R. Soc. London, Ser. A*, **445**(1924), pp. 273–290.
- Murphy, B., and Lorenz, J., 2010, "Simplified Morton Effect Analysis for Synchronous Spiral Instability," *ASME J. Vib. Acoust.*, **132**(5), p. 051008.
- Suh, J., and Palazzolo, A., 2014, "Three-Dimensional Thermohydrodynamic Morton Effect Simulation—Part I: Theoretical Model," *ASME J. Tribol.*, **136**(3), p. 031706.
- Tong, X., and Palazzolo, A., 2016, "Double Overhung Disk and Parameter Effect on Rotordynamic Synchronous Instability-Morton Effect: Part I: Theory and Modeling Approach," *ASME J. Tribol.*, **139**(1), p. 011705.
- Tong, X., Palazzolo, A., and Suh, J., 2016, "Rotordynamic Morton Effect Simulation With Transient, Thermal Shaft Bow," *ASME J. Tribol.*, **138**(3), p. 031705.
- Lee, J., and Palazzolo, A., 2012, "Morton Effect Cyclic Vibration Amplitude Determination for Tilt Pad Bearing Supported Machinery," *ASME J. Tribol.*, **135**(1), p. 011701.
- Lorenz, J., and Murphy, B., 2011, "Case Study of Morton Effect Shaft Differential Heating in a Variable-Speed Rotating Electric Machine," *ASME Paper No. GT2011-45228*.
- Panara, D., Panconi, S., and Griffini, D., 2015, "Numerical Prediction and Experimental Validation of Rotor Thermal Instability," 44th Turbomachinery Symposium, College Station, TX, Sept. 14–17, pp. 1–18.
- Tong, X., Palazzolo, A., and Suh, J., 2017, "A Review of the Rotordynamic Thermally Induced Synchronous Instability (Morton) Effect," *ASME Appl. Mech. Rev.*, epub.
- Schmied, J., Pozivil, J., and Walch, J., 2008, "Hot Spots in Turboexpander Bearings: Case History, Stability Analysis, Measurements and Operational Experience," *ASME Paper No. GT2008-51179*.
- Gomiciaga, R., and Keogh, P., 1999, "Orbit Induced Journal Temperature Variation in Hydrodynamic Bearings," *ASME J. Tribol.*, **121**(1), pp. 77–84.
- Tong, X., and Palazzolo, A., 2016, "The Influence of Hydrodynamic Bearing Configuration on Morton Effect," *ASME Paper No. GT2016-56654*.
- Gadangi, R., Palazzolo, A., and Kim, J., 1996, "Transient Analysis of Plain and Tilt Pad Journal Bearings Including Fluid Film Temperature Effects," *ASME J. Tribol.*, **118**(2), pp. 423–430.
- Heinrich, J., Huyakorn, P., Zienkiewicz, O., and Mitchell, A., 1977, "An 'Upwind' Finite Element Scheme for Two-Dimensional Convective Transport Equation," *Int. J. Numer. Methods Eng.*, **11**(1), pp. 131–143.
- Ettles, C., and Cameron, A., 1968, "Considerations of Flow Across a Bearing Groove," *ASME J. Lubr. Technol.*, **90**(1), pp. 312–319.
- Heshmat, H., and Pinkus, O., 1986, "Mixing Inlet Temperatures in Hydrodynamic Bearings," *ASME J. Tribol.*, **108**(2), pp. 231–244.
- Young, W. C., and Budynas, R. G., 2002, *Roark's Formulas for Stress and Strain*, Vol. 7, McGraw-Hill, New York.
- de Jongh, F., and Van Der Hoeven, P., eds., 1998, "Application of a Heat Barrier Sleeve to Prevent Synchronous Rotor Instability," 27th Turbomachinery Symposium, College Station, TX, Sept. 20–24, pp. 17–26.
- Corcoran, J., Rea, H., and Comejo, G., 1997, "Discovering, the Hard Way, How a High Performance Coupling Influenced the Critical Speeds and Bearing Loading of an Overhung Radial Compressor—A Case History," 26th Turbomachinery Symposium, College Station, TX, Sept. 14–16, pp. 67–78.
- Suh, J., and Palazzolo, A., 2014, "Three-Dimensional Thermohydrodynamic Morton Effect Analysis—Part II: Parametric Studies," *ASME J. Tribol.*, **136**(3), p. 031707.
- Carter, C. R., and Childs, D. W., 2009, "Measurements versus Predictions for the Rotordynamic Characteristics of a Five-Pad Rocker-Pivot Tilting-Pad Bearing in Load-Between-Pad Configuration," *ASME J. Eng. Gas Turbines Power*, **131**(1), p. 012507.
- Kulhanek, C. D., and Childs, D. W., 2012, "Measured Static and Rotordynamic Coefficient Results for a Rocker-Pivot, Tilting-Pad Bearing With 50 and 60% Offsets," *ASME J. Eng. Gas Turbines Power*, **134**(5), p. 052505.
- Childs, D. W., and Saha, R., 2012, "A New, Iterative, Synchronous-Response Algorithm for Analyzing the Morton Effect," *ASME J. Eng. Gas Turbines Power*, **134**(7), p. 072501.